Linearized lattice Boltzmann method for micro- and nanoscale flow and heat transfer

Yong Shi,[1,*] Ying Wan Yap,[2] and John E. Sader[2,†]
[1]*Department of Mechanical, Materials and Manufacturing Engineering, The University of Nottingham Ningbo China, Ningbo 315100, People's Republic of China*
[2]*School of Mathematics and Statistics, The University of Melbourne, Victoria 3010, Australia*
(Received 21 January 2015; published 21 July 2015)

Ability to characterize the heat transfer in flowing gases is important for a wide range of applications involving micro- and nanoscale devices. Gas flows away from the continuum limit can be captured using the Boltzmann equation, whose analytical solution poses a formidable challenge. An efficient and accurate numerical simulation of the Boltzmann equation is thus highly desirable. In this article, the linearized Boltzmann Bhatnagar-Gross-Krook equation is used to develop a hierarchy of thermal lattice Boltzmann (LB) models based on half-space Gaussian-Hermite (GH) quadrature ranging from low to high algebraic precision, using double distribution functions. Simplified versions of the LB models in the continuum limit are also derived, and are shown to be consistent with existing thermal LB models for noncontinuum heat transfer reported in the literature. Accuracy of the proposed LB hierarchy is assessed by simulating thermal Couette flows for a wide range of Knudsen numbers. Effects of the underlying quadrature schemes (half-space GH vs full-space GH) and continuum-limit simplifications on computational accuracy are also elaborated. The numerical findings in this article provide direct evidence of improved computational capability of the proposed LB models for modeling noncontinuum flows and heat transfer at small length scales.

DOI: 10.1103/PhysRevE.92.013307 PACS number(s): 47.11.−j, 47.15.−x, 47.61.−k

I. INTRODUCTION

Rapid advances in nanofabrication over the last few decades have attracted tremendous interest in the field of micro- and nanoscale fluid flows and heat transfer. Fluids—in particular, gases—within micro- and nanoelectromechanical systems are often noncontinuum by nature, and deviate significantly from classical continuum predictions [1,2]. Such deviations can be captured through use of the Boltzmann equation and its kinetic model, e.g., the Boltzmann Bhatnagar-Gross-Krook (BGK) equation [3]. Analytical solution of the Boltzmann equation presents significant challenges and it is thus natural to turn to numerical simulations as a viable and practical approach.

The lattice Boltzmann (LB) method is an established numerical scheme for solving the Boltzmann BGK equation [4,5]. Due to this intrinsic link to the kinetic theory of gases, the LB method has been applied to investigate a large number of micro- and nanoscale fluid flows and heat transfer where the gas mean free path λ is comparable to the device dimension L [5–24], i.e., the finite Knudsen number $\mathrm{Kn} = \lambda/L$. The LB method was originally applied to simulate flows in the continuum limit, where an exact weakly compressible formulation exists. The method has also been applied to noncontinuum flows, first through introduction of kinetic boundary conditions [6] and an effective mean free path [8]. These early models adopted low-order discrete particle velocity sets and have been demonstrated to exhibit reasonable accuracy in simulating slip flows (i.e., $0.01 < \mathrm{Kn} < 0.1$), but suffer from significant errors when applied to transition ($0.1 < \mathrm{Kn} < 10$) and free molecular ($\mathrm{Kn} > 10$) flows. In recent LB studies, growing effort has been paid to constructing high-order LB models using large algebraic precision (AP) quadrature schemes [5,10–15] and the entropic LB formulation [16]. High-order LB models derived from full-space Gaussian Hermite (FGH) quadrature [11–13] are found to describe unbounded flows in the transition flow regime well [12]. For flows bounded by flat walls, however, these models display oscillatory variation in accuracy between even orders and odd orders of quadrature [11]. This unusual behavior is due to discontinuity of the distribution function prescribed by the Maxwell diffusive boundary condition using half-space moments [13]. Conventionally, such an issue has been studied in the context of discrete velocity models in the kinetic theory of gases, where the half-space moment approach was proposed to compute integrals in the diffusive boundary condition through use of half-space quadrature [25–31]. It is found that such an approach achieves good accuracy and fast convergence. The half-space moment approach is also applicable to complex geometries given that a body fitted coordinate system can be easily accommodated in simulation; see Ref. [32]. In line with these developments, a LB model based on half-space Gaussian Hermite (HGH) quadrature was proposed most recently [14]. In comparison to conventional FGH quadrature–based LB models, improvement in computational accuracy and convergence of this model have been observed for simulating noncontinuum isothermal flows bounded by flat walls [14].

The majority of the above progress has been focused on micro- and nanoscale flows under isothermal conditions. In comparison, little work has been done on the LB method for heat transfer at small length scales. Two approaches were developed to incorporate heat transfer effects into the LB framework: the multispeed approach [17–20,33–36] and the double distribution function (DDF) approach [21–24,37–40]. The multispeed approach is based on the Boltzmann equation, which defines a single-particle distribution function and uses its second-order velocity moment to describe the temperature field. To capture thermal effects, such a multispeed LB model employs a larger discrete particle velocity set with

*Corresponding author: Yong.Shi@nottingham.edu.cn
†jsader@unimelb.edu.au

 ©2015 American Physical Society

multiple speeds and an equilibrium distribution with higher-order velocity moments. Sofonea *et al.* [17–20] applied the multispeed approach to simulate micro- and nanoscale heat transfer, specifically thermal transpiration [18]. Interestingly, they used Gauss-Legendre and Gauss-Laguerre quadrature to construct discrete particle velocities in spherical coordinates [19,20]. The resulting multispeed models exhibit reasonable accuracy and fast convergence when applied to transition and ballistic flows and also heat transfer problems. However, the formulation of these LB models is complex (e.g., Ref. [20] adopts a Shakhov collision term for problems with a variable Prandtl number), which limits its general implementation. In contrast, the DDF approach adopts two different distribution functions, together with two relaxation times, to describe the evolution of the velocity and temperature fields, respectively. In so doing, temperature is expressed as the zeroth-order moment of the temperature distribution function and the heat transfer process is simply governed by its BGK-like equation [40]. It has been shown that LB models based on the DDF approach have a simple formulation and are applicable to problems with different Prandtl numbers. Owing to these features, the DDF approach is very popular in simulating continuum heat transfer problems [37–40]. Some studies extend these DDF LB models to simulate heat transfer at small length scales while adding heuristic treatments to mimic noncontinuum effects [21–24]. Nonetheless, such continuum-based DDF LB models lack a rigorous theoretical foundation for modeling noncontinuum heat transfer phenomena, and accuracy of these LB models deteriorates significantly when applied to heat transfer at moderate and large Knudsen numbers. Importantly, no investigation has been conducted to examine the applicability of DDF LB models for micro- and nanoscale noncontinuum heat transfer when equipped with high-order GH-based discrete particle velocity spaces. It also remains unclear whether the accuracy of such LB models can be improved under nonisothermal conditions if they are constructed using HGH quadrature, rather than conventional FGH quadrature.

In this article, we directly tackle these problems and develop a hierarchy of thermal DDF LB models from the linearized Boltzmann BGK equation to simulate noncontinuum flows and heat transfer at the small length scales. This hierarchy is formulated using HGH quadrature ranging from low to high AP. We apply the proposed LB models to simulate thermal Couette flows for a wide range of Knudsen numbers. Through use of high-accuracy direct numerical solutions of the linearized Boltzmann BGK equation [41] as benchmarks, we show the dependence of LB accuracy on HGH quadrature order. We also compare the LB models proposed in this article with (i) those of FGH quadrature–based DDF LB models [13,15] and (ii) simplified DDF LB models in the continuum limit to demonstrate the strength of the LB models proposed here.

The article is organized as follows. In Sec. II, we first derive a linearized thermal kinetic model based on the linearized Boltzmann BGK equation through use of the DDF approach. We then construct its LB algorithms using finite-difference schemes to discretize time and physical space while HGH quadrature is used to discretize particle velocity space in Sec. III. Two simplified versions of the resulting linearized LB algorithm in the continuum limit are also presented in Sec. III. Diffusive boundary conditions on solid boundaries compatible to DDF LB simulation are derived in Sec. IV. In Sec. V, we apply the proposed HGH-based LB algorithms, together with the diffusive boundary conditions, to simulate thermal Couette flows from continuum and slip, through to transition flow regimes. The present numerical results are compared to those using (i) discrete particle velocities based on FGH quadrature and (ii) simplified models in the continuum limit.

II. LINEARIZED DDF THERMAL KINETIC MODEL

In this section, we use the DDF approach to derive a thermal kinetic model based on the linearized Boltzmann BGK equation.

A. Linearized Boltzmann BGK equation

The linearized Boltzmann BGK equation describes the evolution of a perturbation h to the distribution function f from the global Maxwellian f^0, i.e., $h = \frac{f}{f^0} - 1$, in phase space with time due to gas particle streaming and collision [3]:

$$\frac{\partial h}{\partial t} + \mathbf{c}\cdot\frac{\partial h}{\partial \mathbf{r}} = -\frac{1}{\tau}(h - h^{eq}), \tag{1}$$

where t, $\mathbf{r}$, $\mathbf{c}$ and τ represent time, spatial coordinate, particle velocity, and the relaxation time, respectively. The Maxwellian of a gas at a global equilibrium with constant density ρ_0, zero velocity $\mathbf{u} = \mathbf{0}$, and constant temperature T_0 is

$$f^0 = \frac{\rho_0}{(2\pi RT_0)^{D/2}}\exp\left(-\frac{\mathbf{c}^2}{2RT_0}\right), \tag{2}$$

where R is the gas constant and D is the dimensionality of physical space. h^{eq} is a perturbation to local equilibrium f^{eq}, which is defined as $h^{eq} = \frac{f^{eq}}{f^0} - 1$. It can also be formulated by

$$h^{eq} = \frac{\delta\rho}{\rho_0} + \frac{\mathbf{c}\cdot\mathbf{u}}{RT_0} + \left(\frac{\mathbf{c}^2}{2RT_0} - \frac{D}{2}\right)\frac{\delta T}{T_0}, \tag{3}$$

where $\delta\rho$, $\mathbf{u}$, and δT are the fluid density, velocity, and temperature perturbations, which are specified by the moments of h or h^{eq},

$$\delta\rho = \int f^0 h d\mathbf{c} = \int f^0 h^{eq} d\mathbf{c}, \tag{4a}$$

$$\rho_0\mathbf{u} = \int f^0 h\mathbf{c} d\mathbf{c} = \int f^0 h^{eq}\mathbf{c} d\mathbf{c}, \tag{4b}$$

$$\delta T = \frac{1}{\rho_0 DR}\int f^0 h\mathbf{c}^2 d\mathbf{c} - \frac{\delta\rho}{\rho_0}T_0 = \frac{1}{\rho_0 DR}\int f^0 h^{eq}\mathbf{c}^2 d\mathbf{c} - \frac{\delta\rho}{\rho_0}T_0, \tag{4c}$$

The linearized Boltzmann BGK equation, Eq. (1), is valid for all Knudsen numbers. However, this equation characterizes gas relaxation toward local equilibrium by a single time scale τ. Macroscopically, the equation only describes heat transfer at a Prandtl number, Pr = 1.

B. DDF kinetic model

We use the DDF approach to enable solution at arbitrary Pr numbers [38,40]. This approach utilizes the property that momentum and energy carried by gas particles relax towards local equilibrium at different rates [42]. We therefore introduce two distinct relaxation times τ_f and τ_T, corresponding to two perturbation functions h_f and h_T, to characterize particle momentum and energy relaxation, respectively. Mathematically, this results in two linearized equations similar in form to the BGK equation. The first describes particle mass and momentum transport,

$$\frac{\partial h_f}{\partial t} + \mathbf{c}\cdot\frac{\partial h_f}{\partial \mathbf{r}} = -\frac{1}{\tau_f}\left(h_f - h_f^{eq}\right), \tag{5}$$

and the second accounts for particle energy transport,

$$\frac{\partial h_T}{\partial t} + \mathbf{c}\cdot\frac{\partial h_T}{\partial \mathbf{r}} = -\frac{1}{\tau_T}\left(h_T - h_T^{eq}\right), \tag{6}$$

where h_f^{eq} is the same as in Eq. (3) and

$$h_T^{eq} = \frac{\mathbf{c}^2}{DR}h^{eq} = T_0\left[\frac{\delta\rho}{\rho_0}\frac{\mathbf{c}^2}{DRT_0} + \frac{\mathbf{c}\cdot\mathbf{u}}{RT_0}\frac{\mathbf{c}^2}{DRT_0} + \left(\frac{\mathbf{c}^2}{2RT_0} - \frac{D}{2}\right)\frac{\delta T}{T_0}\frac{\mathbf{c}^2}{DRT_0}\right]. \tag{7}$$

Using the two perturbation functions, h_f and h_T, the fluid density, velocity, and temperature perturbations are specified by

$$\delta\rho = \int f^0 h_f d\mathbf{c}, \quad \rho_0\mathbf{u} = \int f^0 h_f \mathbf{c} d\mathbf{c}, \qquad \delta T = \frac{1}{\rho_0}\int f^0 h_T d\mathbf{c} - \frac{\delta\rho}{\rho_0}T_0. \tag{8}$$

Equations (3) and (5)–(8) specify a linearized DDF kinetic model for gas flows and heat transfer. It can be shown that through use of the Chapman-Enskog procedure this model recovers macroscopic linearized continuum equations for Kn $\ll 1$; see Appendix A. Importantly, the resulting Prandtl number, $\mathrm{Pr} = \tau_f/\tau_T$, is specified using appropriate choices for τ_f and τ_T.

III. LINEARZED DDF LB ALGORITHMS

Time, physical space, and particle velocity space of the DDF thermal kinetic model are discretized to formulate the corresponding LB algorithm. For simplicity and without loss of generality, we consider two-dimensional problems in the following discussion.

A. HGH-based DDF LB algorithms

Particle velocity space in Eqs. (5) and (6) is discretized using HGH quadrature [43]. Unlike conventional FGH quadrature, HGH quadrature involves nonzero abscissas only, so that even-order discrete particle velocity spaces will be produced. We specify discrete particle velocities using HGH quadrature with AP = 3,5, and 7, to obtain a hierarchy of the HGH-based discrete particle velocity spaces: D_2Q_{16}, D_2Q_{36}, and D_2Q_{64}; see Appendix B for details.

For each discrete particle velocity space, Eqs. (5) and (6) are rewritten as

$$\frac{\partial h_{f,i}}{\partial t} + \mathbf{c}_i\cdot\frac{\partial h_{f,i}}{\partial \mathbf{r}} = -\frac{1}{\tau_f}\left(h_{f,i} - h_{f,i}^{eq}\right), \tag{9}$$

and

$$\frac{\partial h_{T,i}}{\partial t} + \mathbf{c}_i\cdot\frac{\partial h_{T,i}}{\partial \mathbf{r}} = -\frac{1}{\tau_T}\left(h_{T,i} - h_{T,i}^{eq}\right), \tag{10}$$

where $h_{f,i}$ and $h_{T,i}$ are perturbation functions corresponding to the discrete particle velocity, $\mathbf{c}_i$, and the corresponding local-equilibrium perturbations are

$$h_{f,i}^{eq} = \frac{\delta\rho}{\rho_0} + \frac{\mathbf{c}_i\cdot\mathbf{u}}{c_s^2} + \left(\frac{\mathbf{c}_i^2}{2c_s^2} - \frac{D}{2}\right)\frac{\delta T}{T_0}, \tag{11}$$

$$h_{T,i}^{eq} = T_0\left[\frac{\delta\rho}{\rho_0}\frac{\mathbf{c}_i^2}{Dc_s^2} + \frac{\mathbf{c}_i\cdot\mathbf{u}}{c_s^2}\frac{\mathbf{c}_i^2}{Dc_s^2} + \left(\frac{\mathbf{c}_i^2}{2c_s^2} - \frac{D}{2}\right)\frac{\delta T}{T_0}\frac{\mathbf{c}_i^2}{Dc_s^2}\right], \tag{12}$$

where the sound speed $c_s = \sqrt{RT_0}$.

Next, we discretize time and physical space in Eqs. (9) and (10) using a finite-difference scheme [44]. This yields evolution equations for the two discrete perturbation functions,

$$H_{f,i}^{n+1} + \Delta t\,\mathbf{c}_i\cdot\left(\frac{\partial h_{f,i}^n}{\partial \mathbf{r}}\right)_{\mathrm{FD}} = \left(1 - \frac{\omega_f}{2}\right)h_{f,i}^n + \frac{\omega_f}{2}h_{f,i}^{eq,n}, \tag{13}$$

and

$$H_{T,i}^{n+1} + \Delta t\,\mathbf{c}_i\cdot\left(\frac{\partial h_{T,i}^n}{\partial \mathbf{r}}\right)_{\mathrm{FD}} = \left(1 - \frac{\omega_T}{2}\right)h_{T,i}^n + \frac{\omega_T}{2}h_{T,i}^{eq,n}, \tag{14}$$

where the subscript n represents the nth time layer and Δt is the time step. The dimensionless relaxation frequencies are $\omega_f = \Delta t/\tau_f$ and $\omega_T = \Delta t/\tau_T$. To remove implicitness of the finite-difference scheme [44], two new functions are introduced in Eqs. (13) and (14):

$$H_{f,i} = h_{f,i} + \frac{\omega_f}{2}\left(h_{f,i} - h_{f,i}^{eq}\right), \qquad H_{T,i} = h_{T,i} + \frac{\omega_T}{2}\left(h_{T,i} - h_{T,i}^{eq}\right). \tag{15}$$

The terms $(\partial h_{f,i}^n/\partial\mathbf{r})_{\mathrm{FD}}$ and $(\partial h_{T,i}^n/\partial\mathbf{r})_{\mathrm{FD}}$ on the left-hand side of Eqs. (13) and (14) are finite-difference approximations of spatial gradients of the two perturbation functions. These are evaluated using the second-order upwind scheme to gradients on nodes in the bulk zone (away from solid boundaries), whereas a hybrid scheme constituting first-order upwind and central difference schemes is used for the nodes nearest to solid boundaries [15]. In the fully discrete LB algorithm, the fluid perturbations are

$$\delta\rho = \rho_0\sum_i w_i h_{f,i} = \rho_0\sum_i w_i H_{f,i}, \tag{16a}$$

$$\mathbf{u} = \sum_i w_i h_{f,i}\mathbf{c}_i = \sum_i w_i H_{f,i}\mathbf{c}_i, \tag{16b}$$

$$\delta T = \sum_i w_i h_{T,i} - T_0 \sum_i w_i h_{f,i}$$
$$= \sum_i w_i H_{T,i} - T_0 \sum_i w_i H_{f,i}. \quad (16c)$$

Equations (11)–(16), together with D_2Q_{16}, D_2Q_{36}, and D_2Q_{64}, comprise a hierarchy of linearized HGH-based DDF LB models for simulating micro- and nanoscale flows and heat transfer. Extension from the proposed LB hierarchy to a hierarchy based on FCH quadrature is straightforward—only the discrete particle velocity spaces need to be replaced; e.g., D_2Q_{16} is replaced by $D_2^*Q_{16}$ [15]. Here, the superscript * is used to distinguish full-space and half-space quadratures.

B. Simplified DDF LB algorithms in the continuum limit

LB algorithms developed in the previous section use $h_{T,i}^{eq}$ involving high-order terms in particle velocity, i.e., Eq. (12), which might cause numerical instability in computation [40]. Conventional LB studies usually simplify such a polynomial to a low-order expression by assuming a very small Knudsen number. Here, we present two simplified low-order LB models for the above-specified LB algorithms in the continuum limit (Kn $\ll 1$).

To obtain a low-order expression of $h_{T,i}^{eq}$, we return to the DDF kinetic model and rewrite Eq. (7),

$$h_T^{eq} = h_{T'}^{eq} + R_1 + R_2 + R_3, \quad (17)$$

where

$$h_{T'}^{eq} = T_0\left[\frac{\delta\rho}{\rho_0} + \frac{\delta T}{T_0} + \frac{\mathbf{c}\cdot\mathbf{u}}{RT_0} + \left(\frac{\mathbf{c}^2}{2RT_0} - \frac{D}{2}\right)\frac{\delta T}{T_0}\right], \quad (18)$$

$$R_1 = \frac{\delta\rho}{\rho_0}\left(\frac{\mathbf{c}^2}{DRT_0} - 1\right)T_0, \quad (19)$$

$$R_2 = \frac{\mathbf{c}\cdot\mathbf{u}}{RT_0}\left(\frac{\mathbf{c}^2}{DRT_0} - 1\right)T_0, \quad (20)$$

$$R_3 = \left(\frac{\mathbf{c}^4}{2DR^2T_0^2} - \frac{\mathbf{c}^2}{RT_0} + \frac{D}{2}\right)\delta T. \quad (21)$$

For incompressible flows in the continuum limit, removal of R_1, R_2, and R_3 from Eq. (17) causes a negligible change in thermal conductivity, as we now demonstrate. The expression for thermal conductivity is $k = D/2\tau_T\rho_0R^2T_0$ and not the original $k = (D+2)/2\tau_T\rho_0R^2T_0$; see Appendix C. Numerically, this change in the prefactor of k does not cause any issues in the LB simulation because it can be easily compensated by modifying the relaxation time τ_T. We therefore obtain a simplified discrete local-equilibrium perturbation as a replacement of $h_{T,i}^{eq}$, i.e.,

$$h_{T',i}^{eq} = T_0\left[\frac{\delta\rho}{\rho_0} + \frac{\delta T}{T_0} + \frac{\mathbf{c}_i\cdot\mathbf{u}}{c_s^2} + \left(\frac{\mathbf{c}_i^2}{2c_s^2} - \frac{D}{2}\right)\frac{\delta T}{T_0}\right]. \quad (22)$$

We name the LB algorithm consisting of Eqs. (11), (13)–(16), and (22) as Model SLB-I for convenience.

Equations (11) and (22) have been further simplified in the literature to simulate micro- and nanoscale heat transfer [21–24]. For example, the model in Ref. [23] (we term this SLB-II) uses local-equilibrium perturbations (in the linear form) as

$$h_{f'',i}^{eq} = \frac{\delta\rho}{\rho_0} + \frac{\mathbf{c}_i\cdot\mathbf{u}}{c_s^2}, \quad (23)$$

and

$$h_{T'',i}^{eq} = T_0\left[\frac{\delta\rho}{\rho_0} + \frac{\delta T}{T_0} + \frac{\mathbf{c}_i\cdot\mathbf{u}}{c_s^2}\right], \quad (24)$$

which neglect second-order terms in particle velocity in $h_{f,i}^{eq}$ and $h_{T',i}^{eq}$. Since both simplified models (SLB-I and SLB-II) are theoretically derived in the continuum limit, their application to noncontinuum problems is questionable. In Sec. V, we examine the numerical accuracy of these simplified algorithms for noncontinuum flows and heat transfer, and compare their results to those obtained by the LB algorithm developed in the previous section.

IV. DIFFUSIVE BOUNDARY CONDITION AT SOLID WALLS

We employ the diffusive condition proposed by Maxwell to specify the wall boundary condition. Its original form in terms of the full (nonlinear) distribution function f is [6]

$$f(\mathbf{r}_b,\mathbf{c}) = \frac{\int_{(\mathbf{c}'-\mathbf{u}_b)\cdot\mathbf{n}<0}|(\mathbf{c}'-\mathbf{u}_b)\cdot\mathbf{n}|f(\mathbf{r}_b,\mathbf{c}')d\mathbf{c}'}{\int_{(\mathbf{c}'-\mathbf{u}_b)\cdot\mathbf{n}>0}|(\mathbf{c}'-\mathbf{u}_b)\cdot\mathbf{n}|f^{eq}(\mathbf{r}_b,\mathbf{c}'|\rho_b,\mathbf{u}_b,T_b)d\mathbf{c}'} \times f^{eq}(\mathbf{r}_b,\mathbf{c}|\rho_b,\mathbf{u}_b,T_b), \quad (\mathbf{c}-\mathbf{u}_b)\cdot\mathbf{n} > 0, \quad (25)$$

where $\mathbf{n}$ is the inward unit vector normal to the wall, and ρ_b, $\mathbf{u}_b$, and T_b are the fluid density, wall velocity, and temperature at the position $\mathbf{r} = \mathbf{r}_b$, respectively. To ensure compatibility with the linearized LB algorithms in Sec. III, Eq. (25) is linearized and expressed in terms of h. For a flat wall moving tangentially, i.e., $\mathbf{u}_b\cdot\mathbf{n} = 0$, Eq. (25) becomes

$$h(\mathbf{r}_b,\mathbf{c}) = h^{eq}(\mathbf{r}_b,\mathbf{c}) - \frac{1}{\rho_0}\sqrt{\frac{2\pi}{RT_0}}\left[\int_{\mathbf{c}'\cdot\mathbf{n}<0}(\mathbf{c}'\cdot\mathbf{n})f^0h(\mathbf{r}_b,\mathbf{c}')d\mathbf{c}' + \int_{\mathbf{c}'\cdot\mathbf{n}>0}(\mathbf{c}'\cdot\mathbf{n})f^0h^{eq}(\mathbf{r}_b,\mathbf{c}')d\mathbf{c}'\right], \quad \mathbf{c}\cdot\mathbf{n} > 0. \quad (26)$$

For consistency with the DDF approach, Eq. (26) is rewritten in terms of h_f and h_T. For a specified discrete particle velocity space, we then obtain

$$h_{f,i} = h_{f,i}^{eq} - \sqrt{\frac{2\pi}{RT_0}}\left[\sum_{\mathbf{c}'_i\cdot\mathbf{n}<0} w_{i'}(\mathbf{c}'_i\cdot\mathbf{n})h_{f,i'} + \sum_{\mathbf{c}'_i\cdot\mathbf{n}>0} w_{i'}(\mathbf{c}'_i\cdot\mathbf{n})h_{f,i'}^{eq}\right], \quad \mathbf{c}_i\cdot\mathbf{n} > 0, \quad (27)$$

and

$$h_{T,i} = h_{T,i}^{eq} - \frac{\mathbf{c}_i^2}{DR}\sqrt{\frac{2\pi}{RT_0}}\left[\sum_{\mathbf{c}'_i\cdot\mathbf{n}<0} w_{i'}(\mathbf{c}'_i\cdot\mathbf{n})h_{f,i'} + \sum_{\mathbf{c}'_i\cdot\mathbf{n}>0} w_{i'}(\mathbf{c}'_i\cdot\mathbf{n})h_{f,i'}^{eq}\right], \quad \mathbf{c}_i\cdot\mathbf{n} > 0. \quad (28)$$

Equations (27) and (28) are the required diffusive boundary conditions on solid walls that are compatible with the linearized DDF LB model proposed in Sec. III A. The boundary conditions for SLB-I and SLB-II are identical to Eqs. (27) and

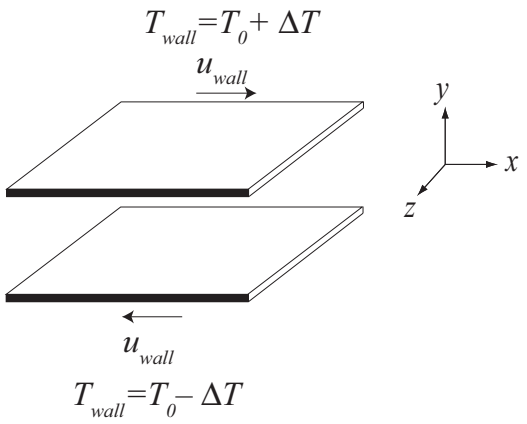

FIG. 1. Schematic of geometry of thermal Couette flow. Origin of the coordinates system is at the center between the plates.

(28), but the used local-equilibrium perturbations for SLB-I are $h^{eq}_{f,i}$ and $h^{eq}_{T',i}$ whereas for SLB-II these variables are $h^{eq}_{f'',i}$ and $h^{eq}_{T'',i}$, respectively.

V. NUMERICAL SIMULATION AND DISCUSSION

In this section, we apply the above-specified linearized DDF LB models to simulate thermal Couette flows, ranging from continuum, slip, through to transition flow regimes. Figure 1 gives a schematic of thermal Couette flow, where two parallel plates separated by a distance L move in opposite directions along their planes with identical speed u_{wall}. Uniform temperatures are applied to each plate with different magnitudes: the top plate has a temperature $T_0 + \Delta T$ while the temperature of the bottom plate is $T_0 - \Delta T$, where ΔT represents a departure to the wall temperature from the global equilibrium temperature T_0.

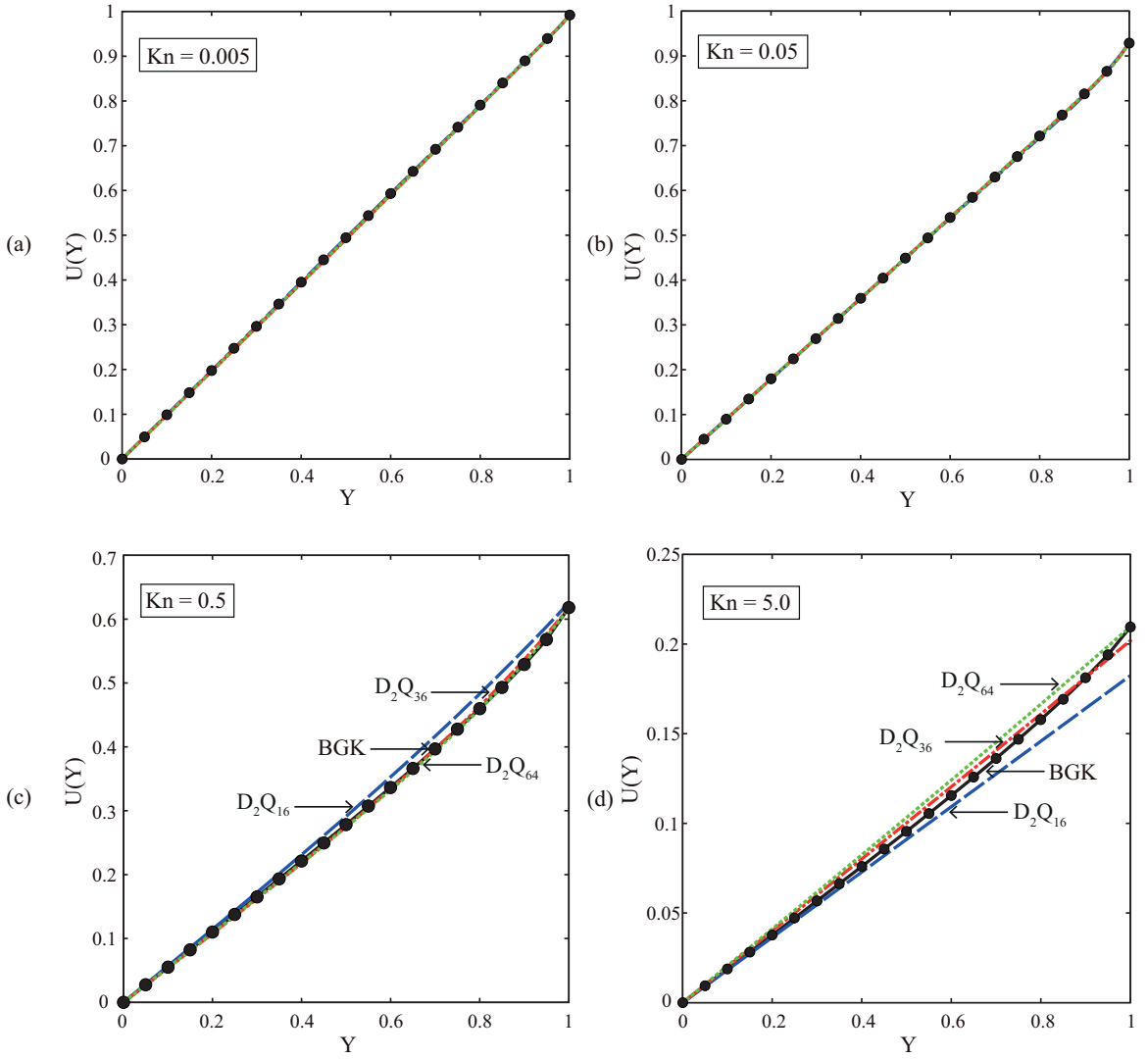

FIG. 2. (Color online) Dimensionless streaming velocity fields ($U = u/u_{\text{wall}}$) of thermal Couette flows for different Knudsen numbers. Solid circle (black): high-accuracy linearized BGK solution [41]; dashed line (blue): D_2Q_{16}; dash-dotted line (red): D_2Q_{36}; dotted line (green): D_2Q_{64}.

Clearly, thermal Couette flow is an ideal problem where its shear (velocity field) and thermal (temperature distribution) effects completely decouple. However, as the first and fundamental canonical problem, we chose this flow in our simulations because high-accuracy direct numerical solutions to the Boltzmann BGK equation can be obtained using the methodology of Ref. [41]. These high-accuracy solutions [41] are used as benchmarks to precisely assess the performance of the LB method for noncontinuum flows and heat transfer at a wide range of Knudsen numbers. More simulations associated with shear-thermal coupling noncontinuum phenomena, such as thermal transpiration, are left for future work. To be specific, three assessments are performed in this article:

(1) Examine the accuracy of the HGH-based LB hierarchy, D_2Q_{16}, D_2Q_{36}, and D_2Q_{64}, for gas heat transfer ranging from continuum to transition flow regimes;

(2) Explore the influence of quadrature scheme (HGH vs FGH) on the accuracy of the LB simulations;

(3) Verify the continuum-limit simplification by comparison of SLB-I and SLB-II to the proposed LB model using $h^{eq}_{T,i}$ given by Eq. (12) and the above-mentioned high-accuracy solutions [41].

LB simulations for thermal Couette flows with Knudsen numbers ranging from 0.005 to 5 across continuum and slip to transition regimes are performed. To nondimensionalize the results, we set the plate separation $L = 1$, reference density $\rho_0 = 1$, plate speed $u_{\text{wall}} = 1$, equilibrium temperature $T_0 = 1$, and temperature perturbation $\Delta T = 0.1$. The discrete diffusive boundary conditions in Sec. IV are specified at the solid walls while periodic boundary conditions are applied in the x direction. All LB simulations are performed on a uniform 120×120 grid with the Mach number $M = 0.16$ and the Courant-Friedrichs-Lewey number $0.03 \leqslant \text{CFL} \leqslant 0.1$. The convergence reaches when $|U_{N+15\,000} - U_N| \leqslant 10^{-4}$, where U_N represents the velocity at the Nth time step. To allow for comparison with the high-accuracy direct solutions of the linearized Boltzmann BGK equation, which involves only a single relaxation time [41], the Prandtl number, Pr, is set to 1.0 in simulation.

A. Numerical results for HGH-based linearized LB hierarchy

Figure 2 shows the streamwise velocities (component in the x direction) as a function of y, obtained using the

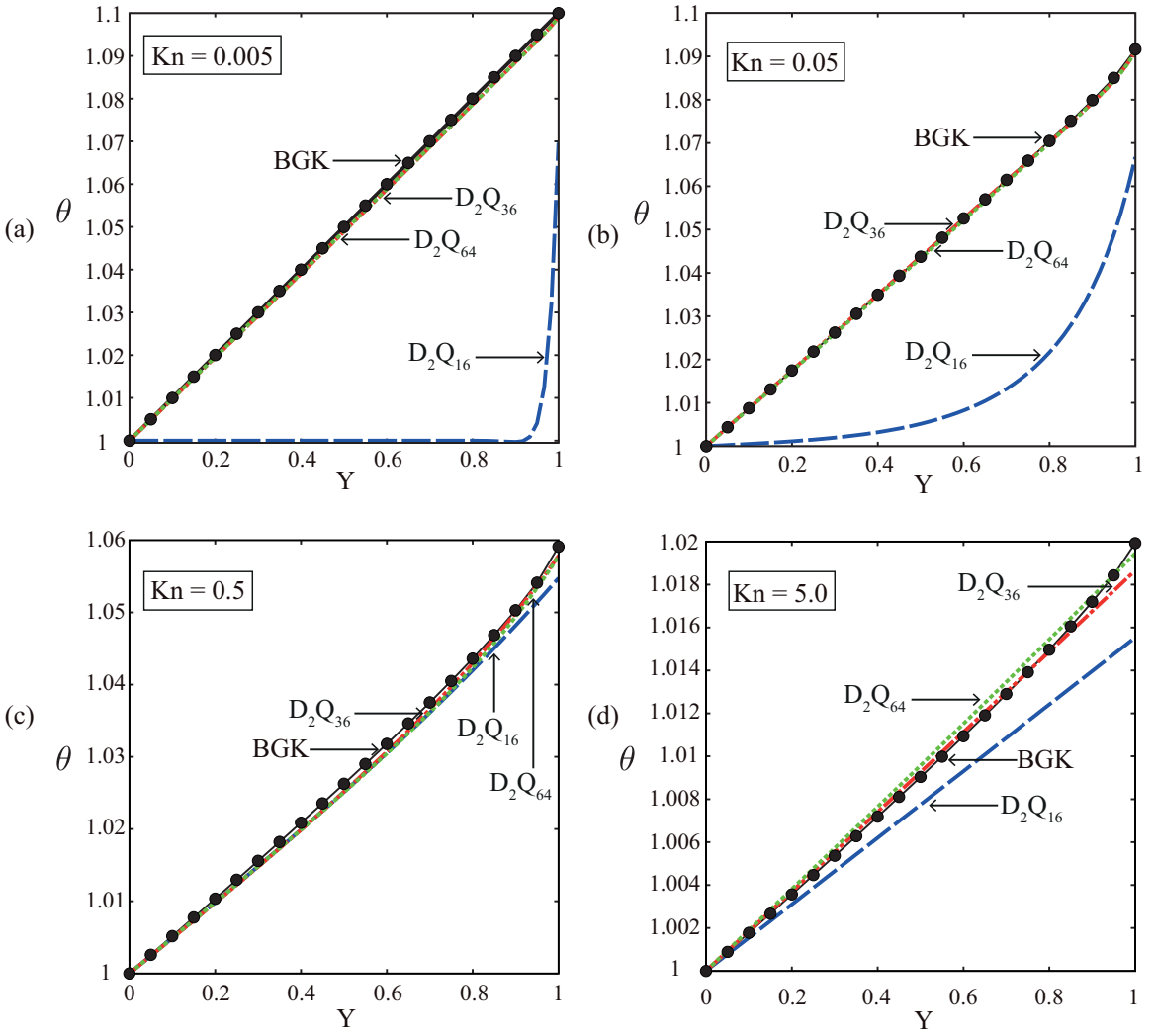

FIG. 3. (Color online) Dimensionless temperature distribution ($\theta = T/T_0$) of thermal Couette flows for a range of Knudsen numbers; details as in Fig. 2.

proposed linearized HGH quadrature–based LB models at Kn = 0.005, 0.05, 0.5, and 5, respectively. Due to the intrinsic symmetry in the flow, numerical results for the top half of the channel, i.e., $0 \leqslant Y \leqslant 1$, are presented, where the dimensionless distance $Y = 2y/L$. From Figs. 2(a) and 2(b), we observe that velocity fields in the continuum and slip regimes given by the HGH quadrature–based LB models are in good agreement with high-accuracy direct solutions of the linearized Boltzmann BGK equation [41]. For transition flows, computational accuracy of the proposed models varies predominantly with the AP of the underlying HGH quadrature. We observe in Figs. 2(c) and 2(d) that the higher the AP, the higher the accuracy of the model. In particular, we note in Fig. 2(c) that the half-space D_2Q_{36} and D_2Q_{64} models recover the nonlinear velocity profile in the Knudsen layer for a transition flow at a moderate Kn. None of the conventional FGH quadrature–based LB models obtain such a nonlinear profile; see Fig. 4 for a detailed comparison. These findings are consistent with previous HGH quadrature-based LB results for isothermal Couette flows [14]. It remains to be seen whether the temperature profiles display a similar variation in accuracy as the discrete particle velocity space is increased.

The corresponding temperature profiles for a range of Knudsen numbers are given in Fig. 3. In the continuum (Kn = 0.005) and slip (Kn = 0.05) regimes, we observe that the thermal LB models accurately predict the temperature distribution, apart from the low-order D_2Q_{16} model; see Figs. 3(a) and 3(b). This is because the quadrature AP of D_2Q_{16} is too small (AP = 3) to allow for accurate evaluation of the high-order moments in the particle velocity space of h_T^{eq}. It is known that these moments are dominant in continuum and slip (near-continuum) flows [5].

Interestingly, Figs. 3(c) and 3(d) show that results using D_2Q_{16} substantially improve when flow is in the transition flow regime. They also show that both D_2Q_{36} and D_2Q_{64} display good accuracy at moderate Knudsen numbers. Importantly, we find that accuracy of the temperature distributions obtained using the proposed HGH quadrature–based LB hierarchy varies monotonically as the discrete particle velocity space expands with increasing quadrature AP. Again, the D_2Q_{64}

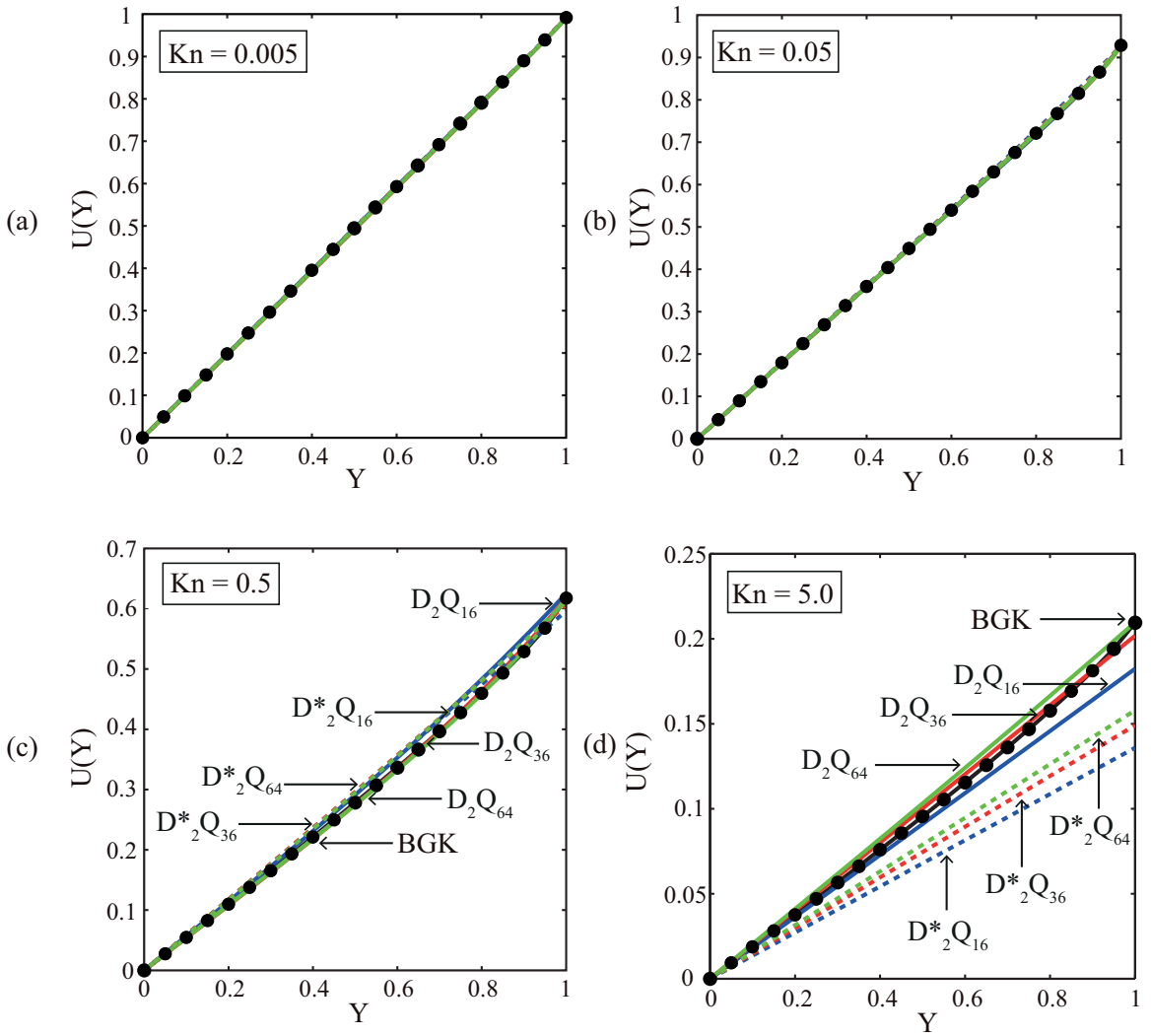

FIG. 4. (Color online) Comparison of streaming velocities obtained by FGH- and HGH-based LB models. Solid circle: high-accuracy linearized BGK solution; blue solid line: D_2Q_{16}; blue dashed line: $D_2^*Q_{16}$; red solid line: D_2Q_{36}; red dashed line: $D_2^*Q_{36}$; green solid line: D_2Q_{64}; green dashed line: $D_2^*Q_{64}$.

LB model, corresponding to the highest AP in the hierarchy, exhibits the best accuracy. Temperature distributions in Fig. 3 together with the velocity profiles in Fig. 2 demonstrate that linearized DDF LB models developed from higher-AP HGH quadrature are capable of simulating flows and heat transfer in continuum, slip, and transition regimes.

B. Effect of quadrature scheme—HGH vs FGH

Conventionally, the particle velocity space is specified through use of FGH quadrature [45]. FGH quadrature is also used to calculate half-space moments in the Maxwell diffusive boundary condition. However, it has been observed previously that discretizing the boundary condition in this way causes numerical inaccuracy in LB simulation of noncontinuum isothermal flows, especially in the Knudsen layer near the walls [11,13]. Most recently, the concept of discretizing particle velocities using HGH quadrature has been proposed to rectify this issue [14]. In this section, we will examine use of FGH and HGH quadratures for heat transfer problems ranging from the continuum to transition regimes. Numerical accuracy of the LB models based on both quadrature rules for thermal Couette flows are again assessed using high-accuracy direct solutions of the linearized Boltzmann BGK equation [41].

We perform FGH quadrature–based LB simulations using the same numerical settings as in Sec. V A, but now with discrete particle velocity spaces replaced with $D_2^*Q_{16}$, $D_2^*Q_{36}$, and $D_2^*Q_{64}$ [15]. Figure 4 shows the velocities obtained for Knudsen numbers ranging from 0.005 to 5, compared with (i) the numerical results of HGH quadrature–based LB models (Fig. 2), and (ii) high-accuracy direct solution of the Boltzmann BGK equation [41]. As shown in Figs. 4(a) and 4(b), the two LB hierarchies well describe gas flows in the continuum and slip regimes. Numerical results for both FGH and HGH are in good agreement with direct solutions, illustrating that quadrature effects exert a negligible effect on the velocity fields for small Kn. Nonetheless, differences among the LB models in these two hierarchies are evident for larger Knudsen number. Figures 4(c) and 4(d) show that accuracy of the LB models in each hierarchy increases monotonically as the discrete particle velocity space expands. Importantly, a comparison between the two hierarchies demonstrates that the HGH quadrature–based hierarchy displays superior accuracy to its FGH quadrature–based counterpart. This is particularly

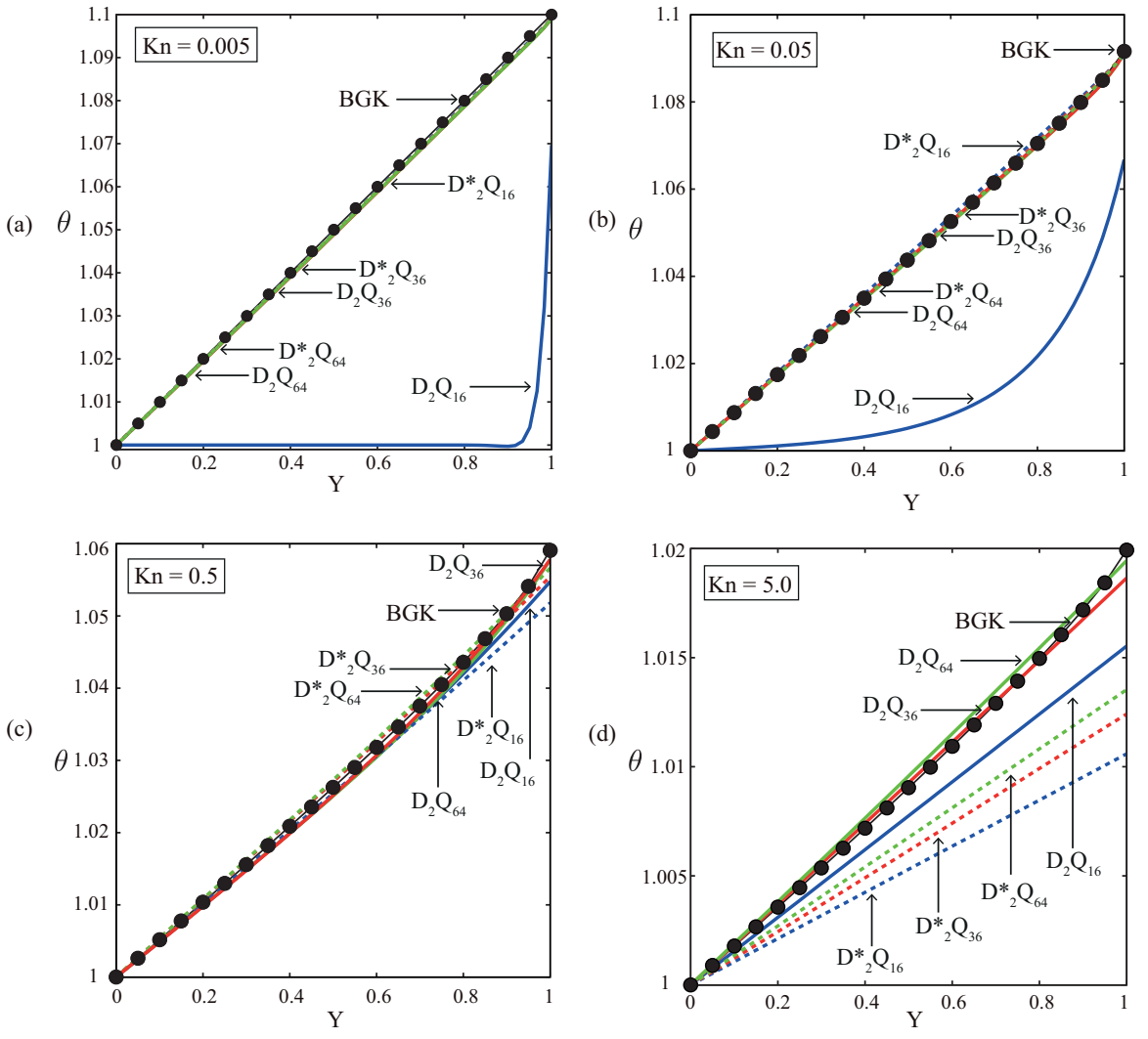

FIG. 5. (Color online) Comparison of temperature distributions obtained by FGH- and HGH-based LB models; details as in Fig. 4.

noticeable at higher Kn: In Fig. 4(d) (Kn = 5.0), even the lowest-order HGH quadrature–based model D_2Q_{16} exhibits greater accuracy than the highest-order model $D_2^*Q_{64}$ in the present FGH quadrature–based hierarchy.

The corresponding temperature distributions obtained using these two LB hierarchies are given in Fig. 5, together with high-accuracy solutions of the Boltzmann BGK equation [41]. Interestingly, the FGH quadrature–based $D_2^*Q_{16}$ achieves better accuracy for the temperature in the continuum and slip regimes than the corresponding HGH quadrature–based D_2Q_{16}. This phenomenon is due to the fact that $D_2^*Q_{16}$ is derived from a FGH quadrature at AP = 7, enabling the evaluation of high-order moments of h_T^{eq} accurately in continuum and slip problems. However, the situation reverses in the transition regime, where the proposed HGH quadrature–based LB hierarchy gives greater accuracy than the conventional FGH quadrature–based models; see Figs. 5(c) and 5(d). This demonstrates that boundary effects described by half-space moments are dominant in transition regime heat transfer at finite Knudsen numbers. Numerical results in Figs. 4 and 5 demonstrate that the HGH quadrature–based LB hierarchy proposed in this article possesses superior capability to LB models based on conventional FGH quadrature for simulating noncontinuum flows and heat transfer.

C. Effects of the continuum-limit simplification

Finally, we compare results obtained using the proposed LB models with $h_{T,i}^{eq}$ given by Eq. (12), and the simplified models formulated in the continuum limit, i.e., models SLB-I and SLB-II. All LB simulations adopt D_2Q_{36} as the discrete velocity space, because the difference between these results and that using D_2Q_{64} is small; results for D_2Q_{16} are very different by comparison. Interestingly, the velocity fields obtained by the simplified models are found to be very similar to those derived using the proposed linearized LB model (in Fig. 2). The agreement in the streamwise velocity among the three models indicates that the modification of $h_{f'',i}^{eq}$ in Eq. (23) does not substantially diminish accuracy in the velocity fields. This observation can be explained by the fact that shear and thermal effects decouple in thermal Couette flows.

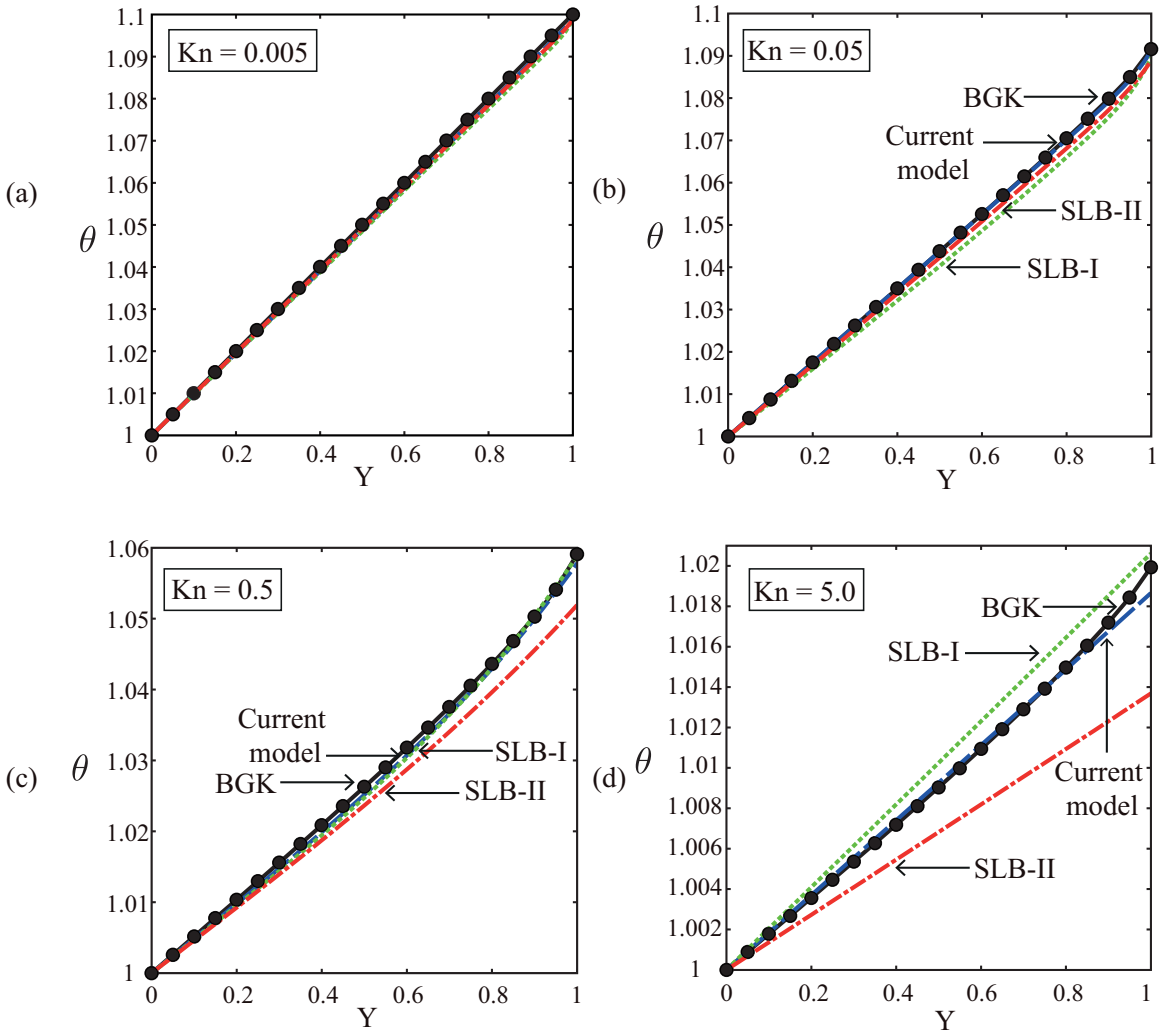

FIG. 6. (Color online) Comparison of temperature distributions given by the three LB models for different Knudsen numbers. The discrete particle velocity spaces used in all models are D_2Q_{36}. Solid circle (black): high-accuracy solution to the linearized Boltzmann BGK equation [41]; dashed (blue): the proposed current LB model; dotted (green): model SLB-I; dash-dot (red): model SLB-II.

Figure 6 gives a comparison of temperature distributions obtained using (i) SLB-I, SLB-II; (ii) the current LB model with $h_{T,i}^{eq}$ given by Eq. (12); and (iii) high-accuracy direct numerical solutions of the linearized Boltzmann BGK equation [41]. The temperature profiles obtained using the three LB models are in close agreement for small-Kn thermal flows, e.g., Kn = 0.005 in Fig. 6(a) and Kn = 0.05 in Fig. 6(b); all numerical results are in good agreement with the high-accuracy solution of the linearized Boltzmann BGK equation. However, deviations in the temperature distributions are observed when simulations are extended to transition heat transfer. Figures 6(c) and 6(d) show that accuracy of the simplest model, SLB-II, which is used conventionally, deteriorates strongly in this regime. SLB-I maintains good accuracy at moderate Knudsen numbers, but overestimates the temperature profiles in thermal flows with large Knudsen numbers. In contrast, the current linearized LB models exhibit superior accuracy to these simplified models over the whole transition flow regime from moderate to large Knudsen numbers. The results in Fig. 6 demonstrate that direct use of the DDF LB formulations developed for continuum flows and heat transfer (i.e., SLB-I and SLB-II) provides poor accuracy for Knudsen numbers larger than unity. These numerical simulations, together with those of Secs. V A and V B, show that accuracy of the LB method depends not only on the underlying quadrature order, but also on use of a high-order local temperature perturbation, i.e., $h_{T,i}^{eq}$.

VI. CONCLUSIONS

A hierarchy of linearized thermal LB models, ranging from D_2Q_{16} to D_2Q_{64}, was developed to simulate noncontinuum heat transfer over a wide range of Knudsen numbers. The models are derived from the linearized Boltzmann BGK equation and adopt two perturbation functions and relaxation times to describe fluid flow and heat transfer, respectively. In contrast to previous studies, the proposed LB models utilize local-equilibrium perturbations having high-order terms in particle velocity, and discretize particle velocity spaces based on half-space GH quadrature.

Accuracy of the proposed linearized thermal LB hierarchy was examined by simulating thermal Couette flows in the continuum, slip, and transition flow regimes. Our numerical simulations demonstrate that the proposed LB models well describe continuum and slip heat transfer, and can achieve reasonable accuracy in the transition regime. The results reveal that the accuracy of the HGH quadrature–based LB models increases monotonically with increasing AP. Importantly, use of HGH quadrature is found to improve LB accuracy substantially for noncontinuum problems as compared to conventional FGH quadrature. The numerical results in this article also show that the continuum-limit simplification, which has been widely used in the previous DDF LB studies, does not enable accurate simulation of noncontinuum heat transfer. Large errors are exhibited in the corresponding LB simulation of transitional heat transfer, although it has a simple low-order formulation. In contrast, the HGH quadrature–based linearized DDF LB method developed here provides a more accurate framework for modeling heat transfer from continuum to transition flow regimes.

ACKNOWLEDGMENTS

Y.S. would like to acknowledge support from the Ningbo Natural Science Foundation (Grant No. 2013A610133) and Ningbo Science and Technology Bureau Technology Innovation Team (Grant No. 2011B81006). Y.W.Y. and J.E.S. gratefully acknowledge support from the Australian Research Council Grant Scheme.

APPENDIX A: DERIVATION OF THE LINEARIZED NAVIER-STOKES EQUATIONS FOR FLOWS AND HEAT TRANSFER USING THE LINEARIZED DDF KINETIC MODEL

In this Appendix, we derive the linearized Navier-Stokes equations for flows and heat transfer from the proposed linearized DDF kinetic model. We first apply the Chapman-Enskog multiscale expansion to the two perturbation functions, temporal and spatial gradients,

$$h_f = h_f^{(0)} + \mathrm{Kn} h_f^{(1)} + \mathrm{Kn}^2 h_f^{(2)} + \cdots, \tag{A1}$$

$$h_T = h_T^{(0)} + \mathrm{Kn} h_T^{(1)} + \mathrm{Kn}^2 h_T^{(2)} + \cdots, \tag{A2}$$

$$\frac{\partial}{\partial t} = \mathrm{Kn}\frac{\partial_1}{\partial t} + \mathrm{Kn}^2\frac{\partial_2}{\partial t} + \cdots, \tag{A3}$$

$$\frac{\partial}{\partial \mathbf{r}} = \mathrm{Kn}\frac{\partial_1}{\partial \mathbf{r}} + \cdots. \tag{A4}$$

We then substitute Eqs. (A1)–(A4) into Eqs. (5) and (6), and obtain a series of equations for different orders of Knudsen number,

$$\mathrm{Kn}^0:\ h_f^{(0)} = h_f^{eq}, \tag{A5}$$

$$\mathrm{Kn}^1:\ \frac{\partial_1 h_f^{(0)}}{\partial t} + \mathbf{c}\cdot\frac{\partial_1 h_f^{(0)}}{\partial \mathbf{r}} = -\frac{1}{\tau_f} h_f^{(1)}, \tag{A6}$$

$$\mathrm{Kn}^2:\ \frac{\partial_1 h_f^{(1)}}{\partial t} + \frac{\partial_2 h_f^{(0)}}{\partial t} + \mathbf{c}\cdot\frac{\partial_1 h_f^{(1)}}{\partial \mathbf{r}} = -\frac{1}{\tau_f} h_f^{(2)}, \tag{A7}$$

and

$$\mathrm{Kn}^0:\ h_T^{(0)} = h_T^{eq}, \tag{A8}$$

$$\mathrm{Kn}^1:\ \frac{\partial_1 h_T^{(0)}}{\partial t} + \mathbf{c}\cdot\frac{\partial_1 h_T^{(0)}}{\partial \mathbf{r}} = -\frac{1}{\tau_T} h_T^{(1)}, \tag{A9}$$

$$\mathrm{Kn}^2:\ \frac{\partial_1 h_T^{(1)}}{\partial t} + \frac{\partial_2 h_T^{(0)}}{\partial t} + \mathbf{c}\cdot\frac{\partial_1 h_T^{(1)}}{\partial \mathbf{r}} = -\frac{1}{\tau_T} h_T^{(2)}. \tag{A10}$$

We next compute the moments of $h_f^{(j)}$ and $h_T^{(j)}$. With the help of Eqs. (3), (7), and (8), we obtain

$$\int f^0 h_f^{eq} d\mathbf{c} = \delta\rho, \quad \int f^0 h_f^{(j)} d\mathbf{c} = 0, \quad j = 1,2,\ldots, \tag{A11}$$

$$\int f^0 h_f^{eq} \mathbf{c} d\mathbf{c} = \rho_0 \mathbf{u}, \quad \int f^0 h_f^{(j)} \mathbf{c} d\mathbf{c} = \mathbf{0}, \quad j = 1,2,\ldots, \tag{A12}$$

$$\int f^0 h_f^{eq} \mathbf{cc} d\mathbf{c} = \delta p \mathbf{I}, \tag{A13}$$

$$\int f^0 h_f^{eq} \mathbf{ccc} d\mathbf{c} = \rho_0 R T_0 \mathbf{u} \cdot \mathbf{\Delta}, \tag{A14}$$

and

$$\int f^0 h_T^{eq} d\mathbf{c} = \delta\rho T_0 + \rho_0 \delta T, \quad \int f^0 h_T^{(j)} d\mathbf{c} = 0, \quad j = 1,2,\cdots, \tag{A15}$$

$$\int f^0 h_T^{eq} \mathbf{c} d\mathbf{c} = \frac{5}{3}\rho_0 T_0 \mathbf{u}, \tag{A16}$$

$$\int f^0 h_T^{eq} \mathbf{cc} d\mathbf{c} = \frac{5}{3}\delta\rho R T_0^2 \mathbf{I} + \frac{10}{3}\rho_0 R T_0 \delta T \mathbf{I}, \tag{A17}$$

where $\delta p = \delta\rho R T_0 + \rho_0 R \delta T$, the second-rank isotropic tensor $\mathbf{I} = \delta_{\alpha\beta}$, and the forth-rank isotropic tensor $\mathbf{\Delta} = \delta_{\alpha\beta}\delta_{\gamma\eta} + \delta_{\alpha\gamma}\delta_{\beta\eta} + \delta_{\alpha\eta}\delta_{\beta\gamma}$. The symbol $\delta_{\alpha\beta}$ is the Kronecker delta and the subscripts α,β,γ, and η represent the Cartesian coordinates.

We recover the macroscopic equations at various order of Kn from Eqs. (A6) and (A7), and (A9) and (A10), through use of the Chapman-Enskog procedure. We multiply both the sides of Eq. (A6) by f^0 and $f^0\mathbf{c}$, respectively, and integrate the obtained equations over the entire particle velocity space. It follows that

$$\frac{\partial_1}{\partial t}\delta\rho + \frac{\partial_1}{\partial \mathbf{r}} \cdot (\rho_0 \mathbf{u}) = 0, \tag{A18}$$

$$\frac{\partial_1}{\partial t}(\rho_0 \mathbf{u}) + \frac{\partial_1}{\partial \mathbf{r}}(\delta p) = 0. \tag{A19}$$

Similarly, we adopt the same steps for Eq. (A9), but multiply the equation only by f^0. With the help of Eqs. (A15) and (A16), the temperature equation at order Kn is derived,

$$\frac{\partial_1}{\partial t}(\rho_0 c_v \delta T) = -p_0 \frac{\partial_1}{\partial \mathbf{r}} \cdot \mathbf{u}, \tag{A20}$$

where $p_0 = \rho_0 R T_0$. The right side of Eq. (A20) represents the compression work.

As to the macroscopic equations of order Kn^2, we multiply both sides of Eq. (A7) by f^0 and $f^0\mathbf{c}$ and Eq. (A10) by f^0, respectively, and integrate the resulting equations over particle velocity space. We then recover

$$\frac{\partial_2}{\partial t}\delta\rho = 0, \tag{A21}$$

$$\frac{\partial_2}{\partial t}(\rho_0 \mathbf{u}) = \mu \frac{\partial_1}{\partial \mathbf{r}} \cdot \left[\frac{\partial_1 \mathbf{u}}{\partial \mathbf{r}} + \left(\frac{\partial_1 \mathbf{u}}{\partial \mathbf{r}}\right)^T\right] - \frac{2}{3}\mu \frac{\partial_1}{\partial \mathbf{r}}\left(\frac{\partial_1}{\partial \mathbf{r}} \cdot \mathbf{u}\right), \tag{A22}$$

and

$$\frac{\partial_2}{\partial t}(\rho_0 c_v \delta T) = \frac{\partial_1}{\partial \mathbf{r}} \cdot \left(k \frac{\partial_1}{\partial \mathbf{r}} \delta T\right), \tag{A23}$$

where the viscosity $\mu = \tau_f \rho_0 R T_0$, heat capacity at constant volume $c_v = 3R/2$, and thermal conductivity $k = \frac{5}{2}\tau_T \rho_0 R^2 T_0$. Combining Eqs. (A18)–(A20) with Eqs. (A21)–(A23), respectively, we obtain the linearized Navier-Stokes equations for flows and heat transfer,

$$\frac{\partial}{\partial t}\delta\rho + \frac{\partial}{\partial \mathbf{r}} \cdot (\rho_0 \mathbf{u}) = 0, \tag{A24}$$

$$\frac{\partial}{\partial t}(\rho_0 \mathbf{u}) = -\frac{\partial}{\partial \mathbf{r}}(\delta p) - \frac{2\mu}{3}\frac{\partial}{\partial \mathbf{r}}\left(\frac{\partial}{\partial \mathbf{r}} \cdot \mathbf{u}\right) + \frac{\partial}{\partial \mathbf{r}} \cdot \left\{\mu\left[\frac{\partial}{\partial \mathbf{r}}\mathbf{u} + \left(\frac{\partial}{\partial \mathbf{r}}\mathbf{u}\right)^T\right]\right\}, \tag{A25}$$

TABLE I. Specifications of D_2Q_{16}, D_2Q_{36}, and D_2Q_{64}. $\mathbf{c}_j$ is the discrete particle velocity and w_j is the corresponding moment weight. a, b, and c denote the velocity components in Cartesian coordinates; these are the products of the quadrature abscissas and $\sqrt{2}c_s$. The subscript, FS, denotes full symmetry.

D_2Q_{16}	$\mathbf{c}_j = \begin{cases}(\pm a, \pm a), & j = 1-4,\\ (\pm b, \pm b), & j = 5-8,\\ (a,b)_{FS}, & j = 9-16.\end{cases}$	$a = 0.42454c_s$, $b = 1.77119c_s$.	$w_{1-4} = 1.306 \times 10^{-1}$, $w_{5-8} = 1.922 \times 10^{-2}$, $w_{9-16} = 5.009 \times 10^{-2}$.
D_2Q_{36}	$\mathbf{c}_j = \begin{cases}(\pm a, \pm a), & j = 1-4,\\ (\pm b, \pm b), & j = 5-8,\\ (\pm c, \pm c), & j = 9-12,\\ (a,b)_{FS}, & j = 13-20,\\ (a,c)_{FS}, & j = 21-28,\\ (b,c)_{FS}, & j = 29-36,\end{cases}$	$a = 0.26948c_s$, $b = 1.19961c_s$, $c = 2.54527c_s$.	$w_{1-4} = 6.333 \times 10^{-2}$, $w_{5-8} = 5.003 \times 10^{-2}$, $w_{9-12} = 6.087 \times 10^{-4}$, $w_{13-20} = 5.629 \times 10^{-2}$, $w_{21-28} = 6.208 \times 10^{-3}$, $w_{29-36} = 5.519 \times 10^{-3}$.
D_2Q_{64}	$\mathbf{c}_j = \begin{cases}(\pm a, \pm a), & j = 1-4,\\ (\pm b, \pm b), & j = 5-8,\\ (\pm c, \pm c), & j = 9-12,\\ (\pm d, \pm d), & j = 13-16,\\ (a,b)_{FS}, & j = 17-24,\\ (a,c)_{FS}, & j = 25-32,\\ (a,d)_{FS}, & j = 33-40,\\ (b,c)_{FS}, & j = 41-48,\\ (b,d)_{FS}, & j = 49-56,\\ (c,d)_{FS}, & j = 57-64.\end{cases}$	$a = 0.18919c_s$, $b = 0.88293c_s$, $c = 1.89864c_s$, $d = 3.19990c_s$.	$w_{1-4} = 3.368 \times 10^{-2}$, $w_{5-8} = 5.645 \times 10^{-2}$, $w_{9-12} = 5.668 \times 10^{-3}$, $w_{13-16} = 1.293 \times 10^{-5}$, $w_{17-24} = 4.360 \times 10^{-2}$, $w_{25-32} = 1.382 \times 10^{-2}$, $w_{33-40} = 6.600 \times 10^{-4}$, $w_{41-48} = 1.789 \times 10^{-2}$, $w_{49-56} = 8.544 \times 10^{-4}$, $w_{57-64} = 2.708 \times 10^{-4}$

and

$$\frac{\partial}{\partial t}(\rho_0 c_v \delta T) = -p_0 \frac{\partial}{\partial \mathbf{r}} \cdot \mathbf{u} + \frac{\partial}{\partial \mathbf{r}} \cdot \left(k \frac{\partial}{\partial \mathbf{r}} \delta T \right). \tag{A26}$$

The Prandtl number $\mathrm{Pr} = \frac{\mu c_p}{k} = \frac{\tau_f}{\tau_T}$.

APPENDIX B: DISCRETE PARTICLE VELOCITY SPACES BASED ON HALF-SPACE GAUSSIAN HERMITE QUADRATURE

We present the three HGH-based discrete particle velocity spaces in this Appendix. We denote each space by $\mathrm{D}_m\mathrm{Q}_n$, where m is the dimensionality of physical space and n is the number of discrete particle velocities. Table I summarizes the mathematical specifications of $\mathrm{D}_2\mathrm{Q}_{16}$, $\mathrm{D}_2\mathrm{Q}_{36}$, and $\mathrm{D}_2\mathrm{Q}_{64}$.

The interested readers can refer to Appendix A in Ref. [15] for specification of the FGH-based discrete particle velocity spaces.

APPENDIX C: SIMPLIFICATION OF h_T^{eq} IN THE CONTINUUM LIMIT

In this Appendix, we prove h_T^{eq} given by Eq. (7) can be simplified to $h_{T'}^{eq}$ [Eq. (18)] in the continuum limit. Equation (7) can be rewritten as

$$h_T^{eq} = h_{T'}^{eq} + R_1 + R_2 + R_3,$$

where R_1, R_2, and R_3 are given by Eqs. (19)–(21). When applying the Chapman-Enskog procedure to recover the continuum temperature equation, we find that only the zeroth- to second-order moments of h_T^{eq} are specified. These low-order moments in terms of R_1, R_2, and R_3 are

$$\int f^0 R_1 d\mathbf{c} = 0, \quad \int f^0 R_1 \mathbf{c} d\mathbf{c} = \mathbf{0},$$
$$\int f^0 R_1 \mathbf{cc} d\mathbf{c} = \frac{2}{3}\delta\rho R T_0^2 \mathbf{I}, \tag{B1a}$$
$$\int f^0 R_2 d\mathbf{c} = 0, \quad \int f^0 R_2 \mathbf{c} d\mathbf{c} = \frac{2}{3}\rho_0 T_0 \mathbf{u},$$
$$\int f^0 R_2 \mathbf{cc} d\mathbf{c} = \mathbf{0}, \tag{B1b}$$
$$\int f^0 R_3 d\mathbf{c} = 0, \quad \int f^0 R_3 \mathbf{c} d\mathbf{c} = \mathbf{0},$$
$$\int f^0 R_3 \mathbf{cc} d\mathbf{c} = \frac{4}{3}\rho_0 R T_0 \delta T \mathbf{I}. \tag{B1c}$$

Only the second-order moments of R_1 and R_3, and the first-order moment of R_2, are nonzero. We show using a Chapman-Enskog analysis that the second-order moments of R_1 and R_3 are only related to thermal conduction in the temperature continuum equation, Eq. (A26). In fact, removing R_1 and R_3 from Eq. (17) only brings about a minor change in thermal conductivity from $k = (D+2)/2\tau_T \rho_0 R^2 T_0$ to $k = D/2\tau_T \rho_0 R^2 T_0$. In simulations, such a change can be easily compensated for by modifying the magnitude of τ_T. As for R_2, its nontrivial first-order moment recovers the compressible work, which is negligibly small for incompressible flows. Therefore, we can neglect R_1, R_2, and R_3 in Eq. (17), and the resulting low-order $h_{T'}^{eq}$ still recovers the correct macroscopic temperature equation for incompressible continuum heat transfer. Its corresponding form in a discrete particle velocity space is $h_{T',i}^{eq}$, which we used in the LB modeling in this article.

[1] G. Karniadakis, A. Beskok, and N. Aluru, *Microflows and Nanoflows: Fundamentals and Simulation* (Springer, New York, 2005).
[2] C. Shen, *Rarefied Gas Dynamics: Fundamentals, Simulation and Micro Flows* (Springer, Berlin, 2005).
[3] C. Cercignani, *Rarefied Gas Dynamics: From Basic Concept to Actual Calculations* (Cambridge University Press, Cambridge,UK, 2000).
[4] X. Shan and X. He, Phys. Rev. Lett. **80**, 65 (1998).
[5] X. Shan, X.-F. Yuan, and H. Chen, J. Fluid Mech. **550**, 413 (2006).
[6] S. Ansumali and I. V. Karlin, Phys. Rev. E **66**, 026311 (2002).
[7] S. Succi, Phys. Rev. Lett. **89**, 064502 (2002).
[8] Y.-H. Zhang, X.-J. Gu, R. W. Barber, and D. R. Emerson, Phys. Rev. E **74**, 046704 (2006).
[9] Y. Shi, T. S. Zhao, and Z. Guo, Phys. Rev. E **76**, 016707 (2007).
[10] S. Ansumali, I. V. Karlin, S. Arcidiacono, A. Abbas, and N. I. Prasianakis, Phys. Rev. Lett. **98**, 124502 (2007).
[11] S. H. Kim, H. Pitsch, and I. D. Boyd, J. Comput. Phys. **227**, 8655 (2008).
[12] J. Meng and Y. Zhang, J. Comput. Phys. **230**, 835 (2011).
[13] Y. Shi, P. L. Brookes, Y. W. Yap, and J. E. Sader, Phys. Rev. E **83**, 045701 (2011).
[14] G. P. Ghiroldi and L. Gibelli, Commun. Comput. Phys. **17**, 1007 (2015).
[15] Y. Shi, Y. W. Yap, and J. E. Sader, Phys. Rev. E **89**, 033305 (2014).
[16] W. P. Yudistiawan, S. K. Kwak, and D. V. Patil, and S. Ansumali, Phys. Rev. E **82**, 046701 (2010).
[17] V. Sofonea and R. F. Sekerka, Phys. Rev. E **71**, 066709 (2005).
[18] V. Sofonea, Phys. Rev. E **74**, 056705 (2006).
[19] V. E. Ambruş and V. Sofonea, Phys. Rev. E **86**, 016708 (2012).
[20] V. E. Ambruş and V. Sofonea, Phys. Rev. E **89**, 041301(R) (2014).
[21] C. Shu, X. D. Niu, and Y. T. Chew, J. Stat. Phys. **121**, 239 (2005).
[22] Y-H. Zhang, X. J. Gu, R. W. Barber, and D. R. Emerson, Europhys. Lett. **77**, 30003 (2007).
[23] L. Zheng, Z. L. Guo, and B. C. Shi, Europhys. Lett. **82**, 44002 (2008).
[24] G. H. Tang, Y. H. Zhang, X. J. Gu, R. W. Barber, and D. R. Emerson, Phys. Rev. E **79**, 027701 (2009).
[25] E. P. Gross, E. A. Jackson, and S. Ziering, Ann. Phys. **1**, 141 (1957).
[26] E. P. Gross and S. Ziering, Phys. Fluids **2**, 701 (1959).
[27] A. B. Huang and R. L. Stoy, Jr., Phys. Fluids **9**, 2327 (1966).
[28] T. Soga, Phys. Fluids **25**, 1978 (1982).
[29] A. Frezzotti, L. Gibelli, and B. Franzelli, Continuum Mech. Thermodyn. **21**, 495 (2009).

[30] L. Gibelli, Phys. Fluids **24**, 022001 (2012).
[31] G. P. Ghiroldi and L. Gibelli, J. Comput. Phys. **258**, 568 (2014).
[32] Z.-H. Li and H.-X. Zhang, Int. J. Numer. Methods Fluids **42**, 361 (2003).
[33] F. J. Alexander, S. Chen, and J. D. Sterling, Phys. Rev. E **47**, R2249 (1993).
[34] Y. Chen, H. Ohashi, and M. Akiyama, Phys. Rev. E **50**, 2776 (1994).
[35] P. Pavlo, G. Vahala, and L. Vahala, J. Stat. Phys. **107**, 499 (2002).
[36] M. Watari and M. Tsutahara, Phys. Rev. E **67**, 036306 (2003).
[37] X. Shan, Phys. Rev. E **55**, 2780 (1997).
[38] X. Y. He, S. Y. Chen, and G. Doolen, J. Comput. Phys. **146**, 282 (1998).
[39] Z. L. Guo, B. C. Shi, and C. G. Zheng, Int. Numer. Methods Fluids **39**, 325 (2002).
[40] Y. Shi, T. S. Zhao, and Z. L. Guo, Phys. Rev. E **70**, 066310 (2004).
[41] J. Nassios, Oscillatory flows of a slightly rarefied gas: A kinetic theory investigation, Ph.D. thesis, The University of Melbourne, 2013.
[42] C. L. Woods, *An Introduction to the Kinetic Theory of Gases and Magnetoplasmas* (Oxford University Press, New York, 1993).
[43] D. Galant, Math. Comput. **23**, 674 (1969).
[44] Z. Guo and T. S. Zhao, Phys. Rev. E **67**, 066709 (2003).
[45] M. Abramowitz and I. A. Stegun, *Handbook of Mathematical Functions with Formulas, Graphs and Mathematical Tables* (Dover, New York, 1972).